East European Journal of Physics. 2. 55–73 (2025)
DOI: 10.26565/2312-4334-2025-2-07 ISSN 2312-4334

GLOBAL COUPLED-CHANNELS PHENOMENOLOGICAL OPTICAL MODEL POTENTIAL FOR NEUTRON - NUCLEUS SCATTERING FROM ^{6}Li TO ^{238}U

Waleed Saleh Alrayashi*
Science Department, Faculty of Education, Sana'a University, Sanna'a, Yemen
*Corresponding Author e-mail: walrayashi@su.edu.ye
Received February 23, 2025; revised March 21, 2025; in final form April 2, 2025; accepted April 12, 2025

The neutron - nucleus scattering process is considered to develop smooth functional forms for the real and imaginary parts of the phenomenological optical potential using the formalism of coupled - channels analysis. We consider intermediate and heavy nuclear targets and investigate the possibility of extending the model to the usually excluded case of light nuclei. Using our model, we simultaneously predict elastic and inelastic angular distributions for neutron scattering from ^{6}Li to ^{238}U for various energies in the range 100 keV $< E <$ 30 MeV for which inelastic angular distributions data are available. We obtain smooth forms for the real and imaginary depths of the volume and surface potential terms as functions of energy, mass number and the asymmetry between the proton and neutron numbers in the target nucleus. The depths of the real and imaginary spin - orbit term, and all the geometry parameters of the potential are fixed. Our predicted elastic and inelastic differential cross sections are in very good agreement with the measured data. The calculated total elastic, total cross sections and the analyzing powers are in a fair overall agreement with the experimental values particularly for the intermediate and heavy nuclei.

Keywords: *Optical model potential; Elastic scattering; Inelastic scattering; Coupled channels; Differential cross section*

PACS: 24.10.Eq, 24.10.Ht, 25.40.Dn, 25.40.Ep, 24.10.-i

1. INTRODUCTION

The optical model describes the complicated interaction between the projectile and target in terms of a complex potential. This potential divides the reaction flux into a real part which corresponds to elastic scattering, and an imaginary part that corresponds to all competing inelastic channels [1]. The main goal of the optical model is to determine potential parameters that can reproduce smooth variations of the scattering differential cross section as a function of the energy of the incident particle and nucleon number of the target nucleus. Although the scattering process may be complicated, noticeable simplification may be achieved if one is only interested in the averaged properties, away from resonances and excitation channels that can be reached by direct reactions. For example, local and also global optical potentials for scattering of nucleons off spherical and approximately spherical nuclei were obtained for incident energies in the range 1 keV to 200 MeV, and target mass numbers that fall in the range $24 \leq A \leq 209$, for which the appropriate experimental data were available [2]. In addition, a global phenomenological optical potential for nucleon scattering off actinides for incident energies up to 300 MeV was developed by considering experimental data for nucleon scattering from ^{232}Th and ^{238}U [3]. Nuclei with charge and mass numbers $89 \leq Z \leq 100$ and $220 \leq A \leq 260$ respectively were included in the study. Furthermore, in Ref. [4], the authors developed optical potentials for medium- and heavy-weight nuclei from ^{54}Fe to ^{238}U corresponding to nucleons incident with energies in the 1 keV to 200 MeV range. Using coupled-channels analysis, the authors obtained smooth systematics for the potential parameters which have simple functional forms. Their results also confirmed that coupled-channels analysis were indispensable to achieving a global description of experimental data for wide ranges of energies and mass numbers $50 \leq A \leq 240$. Other more recent works considered nucleon scattering from light, intermediate and heavy nuclei using a velocity-dependent potential [8] - [11] that reproduced the elastic angular distributions and polarization data to a very good extent, particularly the prominent large angle minima that correspond to nucleon scattering off light $1p$-shell nuclei. Other works modeled the nucleon - nucleus scattering process using the nonlocal Perey and Buck (PB) potential [12] - [14]. The agreement between the predicted angular distributions and experiment was found to be quite satisfactory. Although the PB potential is a nonlocal potential, it was shown that nonlocality alone was not enough to completely describe the proton experimental data, and energy dependent parameters were needed to improve agreement with experiment [15].

In this work, we employ the coupled - channel analysis to develop an optical potential for neutron scattering off various nuclei from ^{6}Li to ^{238}U. This range includes light nuclei: ^{6}Li, ^{12}C and ^{16}O, which are usually excluded when global optical potentials are developed. Their diffuse edges complicate the process of predicting their angular distributions and total cross sections even when local optical potentials are attempted [16]. Despite such difficulties, in this work, we examine the possibility of extending our model to the case of light nuclei. Therefore, in our calculations we consider incident neutrons on nuclei with mass numbers that fall in the range $6 \leq A \leq 238$. The considered nuclei, coupled energy levels and best-fit deformation parameters are given in Table 1. Following the authors of Refs. [3] to [4] and [17], we fix

Cite as: W. S. Alrayashi, East Eur. J. Phys. 2, 55 (2025), https://doi.org/10.26565/2312-4334-2025-2-07

the values of the geometrical parameters and the depths of the spin - orbit term. In addition, we parametrize the real and imaginary parts of the potential as smooth functions of the incident neutron energy, mass number of the target nucleus and the asymmetry between the number of protons and neutrons of the target.

This article is structured as follows. In Section 2 we outline the coupled channels formalism, while Section 3.1 describes the process of deriving our optimal set of parameters. We discuss our results in Section 4. Finally, we present our conclusions in Section 5.

2. COUPLED REACTION CHANNELS FORMALISM

The coupled reaction channels (CRC) is essential for describing scattering processes. When the projectile interacts with the target, the interaction can result in elastic scattering, transitions to excited-state exit channels, or even rearrangement processes. The simplest case occurs when the spin of the target nucleus (I_t) is zero, which is true for even-even nuclei. However, for an odd-A nucleus, I_t is a half-integer, while for an even-A nucleus, I_t is an integer. In elastic scattering, the projectile and the target remain in their ground states after the reaction, and the corresponding Q-value is zero. In this case, the total kinetic energy of the system is conserved in the center-of-mass (C.M.) frame. The scattering potential merely redistributes the outgoing particles without any loss of incident flux. A clear example is:

$$\mathrm{p} + {}^{24}_{12}\mathrm{Mg} \longrightarrow \mathrm{p} + {}^{24}_{12}\mathrm{Mg} \tag{1}$$

In inelastic scattering processes, the kinetic energy of the system is not conserved. Both the projectile and the target retain their identities, but one or both may be excited to higher energy states. Part of the kinetic energy of the relative motion is transferred to internal excitation energy. Inelastic scattering typically occurs when one or both nuclei are deformed. An example of such a process is:

$$\mathrm{p} + {}^{24}_{12}\mathrm{Mg} \longrightarrow \mathrm{p} + {}^{24}_{12}\mathrm{Mg}^{*}(I^{\pi} = 2^{+}, 4^{+}, 6^{+}, \ldots) \tag{2}$$

The coupled-channel theory is a powerful method for incorporating inelastic channels, especially those arising from collective excitations. The formalism was first introduced by Bohr and Mottelson [18], and was later applied by Margolis et al. and Chase et al. [19]. Here, we provide a brief outline of the coupled-channel analysis. A more detailed description can be found in Ref. [20]. In the center-of-mass frame (C.M.), the Schrödinger equation for a nucleon scattered by a target nucleus takes the form:

$$\left[\hat{T}(r) + H(\xi_t) + V(r, \xi_t)\right]\Psi(\vec{r}, \xi_t) = E\Psi(\vec{r}, \xi_t), \tag{3}$$

where r is the radial coordinate from the target to the projectile, and $H(\xi_t)$ is the Hamiltonian for the internal motion of the target, while ξ_t represents the internal coordinates of the target. The interaction potential, $V(r, \xi_t)$ which can be expressed as [20]

$$V(r, \xi_t) = V_{diag} + V_{coupl}, \tag{4}$$

where V_{diag} is a scalar potential that simulates elastic scattering, while V_{coupl} represents the interaction that couples the initial and final states and therefore takes care of inelastic scattering. Further, $\hat{T}(r)$ is the total kinetic energy, which may be written as

$$\hat{T}(r) = -\frac{\hbar^2}{2\mu}\nabla_r^2, \tag{5}$$

where $\mu = \frac{m_p m_t}{m_p + m_t}$ is the reduced mass of the projectile and target, and ∇_r^2 is the Laplacian operator. where, E is the total energy, and $\Psi(\vec{r}, \xi_t)$ is the wave function of the whole system. Now we shall expand $\Psi(\vec{r}, \xi_t)$ in terms of the eigenstates of the total angular momentum $\psi_J^{\pi M}(\vec{r}, \xi_t)$ as follows [20]:

$$\Psi(\vec{r}, \xi_t) = \sum_{\pi J M} A_{JM}\, \psi_J^{\pi M}(\vec{r}, \xi_t), \tag{6}$$

For each channel $[(l_n s) j_n, I_n]$, where J is the total angular momentum of the whole system;

$$\vec{\mathrm{J}} = \vec{\mathrm{j}}_n + \vec{\mathrm{I}}_n, \tag{7}$$

such that $\vec{\mathrm{j}}_n = \vec{l}_n + \vec{\mathrm{s}}$, where l_n is the orbital angular momentum quantum number, s is the spin of the projectile and I_n is the target's spin, M is the projection of J in units of $\hbar$, and the factors A_{JM} are the amplitudes specifying how much of a total angular momentum state is present. In addition, the parity of the whole system has the form:

$$\pi = (-1)^{l_n}\pi_{I_n}, \tag{8}$$

where π_{I_n} is the parity of the target nucleus. Furthermore, we use the expansion

$$\psi_J^{\pi M}(\vec{r},\xi_t) = \sum_{n(l_n s)j_n I_n} \frac{1}{r} R^{\pi J}_{n(l_n s)j_n I_n}(r)\, \Phi^{JM}_{l_n j_n I_n}(\hat{r},\xi_t), \tag{9}$$

The nuclear wave functions are defined as:

$$\begin{aligned}\Phi^{JM}_{l_n j_n I_n}(\hat{r},\xi_t) &= \sum_{m_{j_n} m_{I_n}} \sum_{m_{l_n} m_s} < l_n s\, m_{l_n} m_s \mid j_n m_{j_n} >< j_n I_n m_{j_n} m_{I_n} \mid JM > \\ &\times\ i^{l_n} Y^{m_{l_n}}_{l_n}(\hat{r})\, \chi^{m_s}_s\, \phi^{m_{I_n}}_{I_n}(\xi_t),\end{aligned} \tag{10}$$

where $R^{\pi J}_{nl_n j_n I_n}(r)$ are the radial wave functions, while $Y^{m_{l_n}}_{l_n}(\hat{r})$ are the spherical harmonics. The matrix elements $< l_n s m_{l_n} m_s \mid j_n m_{j_n} >$ are the Clebsch-Gordon coefficients for coupling $l_n m_{l_n}$ and $s m_s$ to an intermediate angular momenta $j_n m_{j_n}$, while the the elements $< j_n I_n m_{j_n} m_{I_n} \mid JM >$ are the Clebsch-Gordon coefficients for coupling $j_n m_{j_n}$ and $I_n m_{I_n}$ to a total of angular momentum JM for the whole system. Finally, $\phi^{m_{I_n}}_{I_n}(\xi_t)$ and $\chi^{m_s}_s$ are the wave functions for the target and projectile, respectively. Now, by substituting Eqs. (6), (9), and (10) into Eq. (3) and noting that

$$H_t(\xi_t)\phi^{m_{I_n}}_{I_n}(\xi_t) = \epsilon_n \phi^{m_{I_n}}_{I_n}(\xi_t), \tag{11}$$

one obtains

$$\sum_{nl_n j_n I_n} \left[\hat{T}_{n\,l_n} + V(r,\xi_t) - E_n\right] R^{\pi J}_{nl_n j_n I_n}(r)\, \Phi^{JM}_{l_n j_n I_n}(\hat{r},\xi_t) = 0, \tag{12}$$

where

$$\hat{T}_{n\,l_n} = \frac{\hbar^2}{2\mu_n}\left[-\frac{d^2}{dr^2} + \frac{l_n(l_n+1)}{r^2}\right], \tag{13}$$

Here, ϵ_n is the eigenenergies for the target, and $E_n = E - \epsilon_n$ is the external energy for a given excited state. Multiplying Eq. (12) by $[\Phi^{JM}_{n' l_{n'} j_{n'} I_{n'}}(\hat{r},\xi_t)]^*$ from the left, and integrating over the internal coordinates except the radial variable r, leads to the following partial wave coupled differential equations:

$$\left[E_n - \hat{T}_{n\,l_n} - V_{diag}(r)\right] R^{\pi J}_{nl_n j_n I_n}(r) = \sum_{n' l_{n'} j_{n'} I_{n'}} \left\langle l_n j_n I_n | V_{coupl} | l_{n'} j_{n'} I_{n'} \right\rangle R^{\pi J}_{n' l_{n'} j_{n'} I_{n'}}(r). \tag{14}$$

The matrix elements for the coupling potential are given by

$$\left\langle l_n j_n I_n | V_{coupl} | l_{n'} j_{n'} I_{n'} \right\rangle = \left\langle [\mathcal{Y}_{l_n j_n}(\hat{r}) \otimes \phi_{I_n}(\xi_t)]^M_J | V_{coupl} | [\mathcal{Y}_{l_{n'} j_{n'}}(\hat{r}) \otimes \phi_{I_{n'}}(\xi_t)]^M_J \right\rangle. \tag{15}$$

Nuclear structure deformations affect the matrix elements on the right-hand side of Eq. (14). For a non-deformed target nucleus, the coupling potential vanishes, and the set of coupled differential equations reduces to that of the Schrödinger equation for a single channel. Deformed nuclei can be described using either the vibrational or rotational models. In this work, we use the optical model and coupled-channel analysis to couple the ground state to collective excited states of the target nucleus.

This coupling introduces off-diagonal elements in the interaction potential matrix, allowing the incident neutron to induce transitions from the ground state to inelastic states such as the 2^+ state at 4.44 MeV in ^{12}C. These coupling potentials, typically derived from nuclear deformation (e.g., using a deformation parameter β), significantly affect observables such as scattering cross sections and resonance structures. As a result, including channel coupling provides a more accurate description of the reaction dynamics, especially for deformed nuclei like ^{12}C.

3. THE OPTICAL POTENTIAL PARAMETERS

For nucleon-nucleus scattering, the phenomenological optical potential, $V(r,E)$, can be expressed as [20]

$$\begin{aligned}V(r,E) &= -\Big(V_v(E) + iW_v(E)\Big) f(r,R_v,a_v) + i4a_s W_s(E)\frac{d}{dr} f(r,R_s,a_s) \\ &+ \Big(V_{so} + iW_{so}\Big)\Big(\frac{\hbar}{m_\pi c}\Big)^2 \frac{1}{r}\frac{d}{dr} f(r,R_{so},a_{so})\vec{L}\cdot\vec{\sigma},\end{aligned} \tag{16}$$

where $V_v(E)$ and V_{so} are the real components of the volume-central and spin-orbit potentials, respectively. In addition, $W_v(E)$, $W_s(E)$ and W_{so} are the respective imaginary components of the volume, surface and spin-orbit potentials. E is the energy of the incident particle in the laboratory frame. The Woods-Saxon potential has the well-known form:

$$f(r,R_i,a_i) = \frac{1}{1+\exp\left[(r-R_i)/a_i\right]}, \quad i = v,s,so. \tag{17}$$

Deformed nuclei whose surfaces vibrate about an equilibrium shape are treated using the vibrational model. Here, the dynamic nuclear radius R_i is taken to be a function of the polar angles θ and ϕ according to:

$$R_i(\theta,\phi) = r_i A^{\frac{1}{3}}\left[1 + \sum_{\lambda\geq 1}^{\infty}\sum_{\mu=-\lambda}^{\mu=\lambda} \alpha_{\lambda\mu} Y_{\lambda\mu}(\theta,\phi)\right], \tag{18}$$

where $R_i(\theta,\phi)$ is the distance from the center of the nucleus to a point at its surface subtending polar and azimuthal angles (θ,ϕ). The spherical tensors $\alpha_{\lambda\mu}$ are the spherical harmonics $(Y_{\lambda\mu}(\theta,\phi))$ coefficients. However, some nuclei have permanent deformations about a symmetry axis and are treated using the rotational model. In this case the nuclear radius is expressed in the form:

$$R_i(\theta') = r_i A^{\frac{1}{3}}\left[1 + \sum_{\lambda} \beta_\lambda Y_{\lambda 0}(\theta')\right], \tag{19}$$

where, θ' is the polar angle in the body - fixed frame and β_λ is the deformation parameter.

When the vibrational or rotational models are used, one has to determine which parts of the potential are to be deformed. Since the nuclear force is a short range force the nuclear potential follows the shape of the nucleus. Therefore, it is a common practice to deform the volume term of the potential. Deforming the imaginary - surface part, however, is a matter of dispute. This issue has been discussed and arguments were presented in support and also against deforming the imaginary surface part [22]. However, in a later work [23], the authors stated that " to describe the inelastic scattering best, it is found necessary to deform the imaginary (as well as the real) part of the central potential". Furthermore, in Ref. [24] the authors used an optical model with channel coupling to analyze nucleon induced reactions. All parts of the nuclear potential were deformed except the spin-orbit term. In Ref. [21] we examined the effect of channel coupling on the variation of the potential parameters corresponding to nucleon scattering off light and heavy nuclei. We obtained excellent angular distribution fits for the elastic and inelastic channels by deforming both the real volume and imaginary surface terms. Therefore, in this work, we shall deform the surface imaginary term in addition to the real volume term. We did not deform the spin - orbit term as the effects of its deformation on the calculated differential cross sections were found to be insignificant [25].

3.1. Global Optical Potential Parameters

Following the parametrization of Refs. [3] and [17], we express the depths of the optical potential as functions of incident energy, the target's mass number and the asymmetry between the numbers of neutrons and protons $(N-Z)$ in the form:

$$\begin{aligned} V_v(E) &= v_0 + v_1 E + v_2 E^2 + v_3\frac{N-Z}{A} + v_4\frac{Z}{A^{\frac{1}{3}}}, \\ W_v(E) &= W_0 + W_1 E + W_2\frac{N-Z}{A}, \\ W_s(E) &= w_0 + w_1 E + w_2 E^2 + w_3\frac{N-Z}{A}, \end{aligned} \tag{20}$$

where N and Z are the neutron and proton numbers of the target nucleus, respectively, and E is the energy of the incident nucleon in the laboratory frame. Using the SFRESCO code [26] we performed a least-square fit analysis to search for best-fit parameters v_i, W_i and w_i that best reproduce the elastic, inelastic and polarization data for each of the considered nuclei. Following the works of Refs. [3], [4] and [17], we fixed the values of the radius and diffuseness parameters r_i and a_i given in Eq. (17) in addition to the values of the real and imaginary depths of the spin-orbit term as follows:

$$\begin{aligned} r_v &= r_s = 1.20 \text{ fm}, \qquad a_v = 0.65 \text{ fm}, \; a_s = 0.60 \text{ fm} \\ r_{so} &= 1.10 \text{ fm}, \qquad a_{so} = 0.60 \text{ fm} \\ V_{so} &= 6.0 \text{ MeV}, \qquad W_{so} = 0.5 \text{ MeV}, \end{aligned} \tag{21}$$

For each nucleus, we determined the values of the central volume and surface absorption depths for each incident energy by fitting the available corresponding elastic and inelastic angular distributions in addition to the polarization data. After determining the best values of the depths in Eq. (20), we used the OriginLab software to determine the optimum values of v_i, W_i and w_i that best describe the variation of the depths as a function of E, A and $N-Z$ as follows:

$$\begin{aligned} V_v(E) &= 53.54 - 0.102E - 0.00879E^2 - 20\frac{N-Z}{A} + 0.0656\frac{Z}{A^{\frac{1}{3}}}, \\ W_v(E) &= 0.6 + 0.14E - 7.4\frac{N-Z}{A}, \end{aligned}$$

$$\begin{aligned} W_s(E) &= 1.697 + 0.303E - 0.0054E^2 + 7.4\frac{N-Z}{A}, \\ W_s(E) &= -1.303 + 0.303E - 0.0054E^2 + 7.4\frac{N-Z}{A}, \quad \text{only for } ^{12}\text{C and}^{16}\text{O}, \end{aligned} \tag{22}$$

The contribution of compound nucleus formation to the scattering process becomes important at low energies. In addition, the low energy data is vital in testing the applicability of an optical potential. Therefore, we tested the accuracy of our model's predictions at low energies using the TALYS computer code [27], which accounts for the compound nucleus formation, but with our values for all the optical potential parameters. As we shall see below, the agreement between our predictions and the experimental data is quite reasonable at incident energies as low as 180 keV.

We note here that the deformation parameters β were included in the fitting procedure. The best fit values are shown in Table 1. The initial values for the deformation parameters were taken from Refs. [23] and [29] to [33].

Table 1. The coupled energy levels and the corresponding best-fit deformation parameter for each considered nucleus.

Target	Coupled levels I^π (Excitation energy in MeV)	deformation parameters
^{6}Li	1^+ (g.s), 3^+(2.186)	β_2=1.1006
^{12}C	0^+ (g.s), 2^+(4.438),	β_2 =0.655
^{16}O	0^+ (g.s), 3^-(6.129), 2^+(6.917)	β_2 = 0.364, β_3= 0.7243
^{24}Mg	0^+ (g.s), 2^+(1.368)	β_2 = 0.499
^{28}Si	0^+ (g.s), 2^+(1.779), 4^+(4.617)	β_2 = 0.40, β_4=0.25
^{32}S	0^+ (g.s), 2^+(2.230)	β_2 = 0.262
^{40}Ca	0^+ (g.s), 3^-(3.736)	β_3 = 0.359
^{51}V	$\frac{7}{2}^-$ (g.s), $\frac{3}{2}^-$(0.982)	β_2 = 0.157
^{52}Cr	0^+ (g.s), 2^+(1.434)	β_2 = 0.223
^{54}Fe	0^+ (g.s), 2^+(1.408)	β_2 = 0.176
^{56}Fe	0^+ (g.s), 2^+(0.846), 4^+(3.122)	β_2=0.243
^{58}Ni	0^+ (g.s), 2^+(1.454)	β_2 = 0.172
^{60}Ni	0^+ (g.s), 2^+(1.332)	β_2 = 0.192
^{63}Cu	$\frac{3}{2}^-$ (g.s), $\frac{7}{2}^-$(1.327)	β_2 = 0.231
^{65}Cu	$\frac{3}{2}^-$ (g.s), $\frac{7}{2}^-$(1.481)	β_2 = 0.228
^{76}Se	0^+ (g.s), 2^+(0.559)	β_2 = 0.256
^{80}Se	0^+ (g.s), 2^+(0.666)	β_2 = 0.230
^{90}Zr	0^+ (g.s), 2^+(2.19)	β_2 = 0.111
^{92}Zr	0^+ (g.s), 2^+(0.935)	β_2 = 0.103
^{94}Mo	0^+ (g.s), 2^+(0.871 MeV)	β_2= 0.176
^{116}Sn	0^+ (g.s), 2^+(1.293)	β_2 = 0.10252
^{118}Sn	0^+ (g.s), 2^+(1.229)	β_2 = 0.111
^{120}Sn	0^+ (g.s), 2^+(1.171)	β_2 =0.08448
^{208}Pb	0^+ (g.s), 3^-(2.615), 5^-(3.197)	β_3 =0.127, β_5= 0.06
^{238}U	0^+ (g.s), 2^+(0.045 MeV), 4^+(0.148 MeV)	β_2 =0.178 , β_4=0.06

The functional forms for the central volume and imaginary surface terms lead to the usual energy dependence as can be concluded by inspecting Fig. 1 that corresponds to neutron incident energy off ^{56}Fe. Clearly, the central potential depth $V_v(E)$ decreases with increasing incident energy, but the absorption term W_s which accounts for inelastic processes increases with energy. This behavior is anticipated as more inelastic channels become available with increasing values of E. In such a case, larger values of W_s are required to account for the increase in the flux that is removed form the elastic channel. It is also worth noting that to improve the description of the experimental data for ^{12}C, ^{16}O we found it necessary to shift W_s down by a constant compared to all the other considered nuclei as can be seen in Eq. (22).

One way to judge the quality of the fit to a given data set is by calculating the χ^2 value, which quantifies the difference between the theoretical angular distributions and the experimental data. For a given nucleus n, the χ^2 value can be defined as:

$$\chi^2_n = \frac{\frac{W_{n,non}}{N_{n,non}}\sum_{i=1}^{N_{n,non}}\left(\frac{\sigma^{th}_{non,i}-\sigma^{exp}_{non,i}}{\Delta\sigma^{exp}_{non,i}}\right)^2 + \frac{W_{n,el}}{N_{n,el}}\sum_{i=1}^{N_{n,el}}\frac{1}{N_{n,i}}\sum_{j=1}^{N_{n,i}}\left(\frac{(\frac{d\sigma(\theta_j)_i}{d\Omega})_{\text{theo}}-(\frac{d\sigma(\theta_j)_i}{d\Omega})_{\text{exp}}}{\Delta(\frac{d\sigma(\theta_j)_i}{d\Omega})}\right)^2}{W_{n,non}+W_{n,el}}, \tag{23}$$

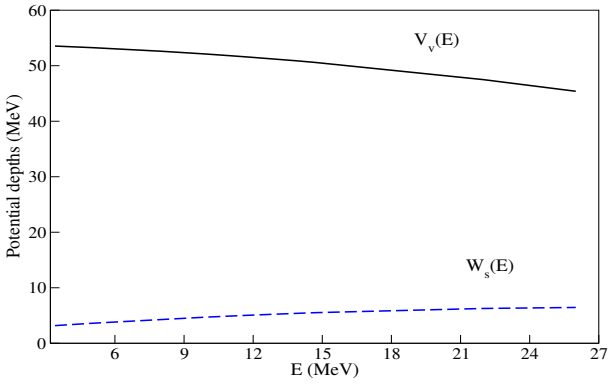

Figure 1. (Color online) Plots of the volume and surface absorption depths as a function of incident energy, see Eq. (22), corresponding to neutron scattering from ^{56}Fe.

where $(\frac{d\sigma(\theta_j)_i}{d\Omega})_{\text{theo}}$ and $(\frac{d\sigma(\theta_j)_i}{d\Omega})_{\text{exp}}$ are the calculated and measured angular distributions corresponding to the j^{th} angular momentum quantum number with the i^{th} incident energy. The subscripts 'el' and 'non' correspond to the elastic and nonelastic angular distribution data sets respectively. In addition, $(\Delta\frac{d\sigma(\theta_j)_i}{d\Omega})$ is the corresponding error on the experimental data, $N_{n,i}$ is the number of experimental data points for the n^{th} nucleus at the i^{th} incident energy. Furthermore, $N_{n,el}$ and $N_{n,non}$ are the numbers of elastic and nonelastic scattering cross section data points for the n^{th} nucleus, while $\sigma^{th}_{non,i}$ and $\sigma^{exp}_{non,i}$ are the calculated and measured nonelastic differential cross sections at the i^{th} incident energy, respectively, and $\Delta\sigma^{exp}_{non,i}$ is the corresponding error on experimental data. Finally, $W_{n,el}$ and $W_{n,non}$ are the weights of the elastic and nonelastic cross sections respectively. In addition, in this work, all the experimental data are assumed to be equally reliable. Equation (22) gives our best-fit global neutron-nucleus potential parameters, that we determined by minimizing the global value χ^2_{global} which is defined as:

$$\chi^2_{global} = \frac{1}{N}\sum_{n=1}^{N}\chi^2_n, \tag{24}$$

where $N = 25$ is the number of the target nuclei shown in Table 1.

Table 2. The χ^2_n values calculated using Eq. (23) for the shown nuclei and the global χ^2_{global} value as defined in Eq. (24) corresponding to our global potential set of parameters given in Eq. (22).

Nucleus	χ^2_n	Nucleus	χ^2_n	Nucleus	χ^2_n
^{6}Li	8.8	^{54}Fe	22.4	^{92}Zr	103
^{12}C	20.7	^{56}Fe	22.2	^{94}Mo	66
^{16}O	12.8	^{58}Ni	30.3	^{116}Sn	7
^{24}Mg	9.5	^{60}Ni	22.3	^{118}Sn	27
^{28}Si	27	^{63}Cu	5	^{120}Sn	12
^{32}S	28	^{65}Cu	3.5	^{208}Pb	30
^{40}Ca	90	^{76}Se	18.8	^{238}U	25
^{51}V	16	^{80}Se	63		
^{52}Cr	9.2	^{90}Zr	23.2		
χ^2_{global}			28.2		

4. RESULTS AND DISCUSSION

In this work, we have used the coupled - channels formalism to obtain an optical potential optimized set of parameters corresponding to neutron scattering from medium and heavy nuclei. We examined the applicability of the model to the case of light nuclei. The experimental elastic and inelastic differential cross section data are obtained from the Experimental Nuclear Reaction Data (EXFORE) [35] and the Computer Index of Nuclear Reaction Data (CINDA) [36]. As we mentioned earlier, for the nuclei considered in this work, all the inelastic angular distribution data in the relevant nuclear data libraries exist for incident neutron energies below 30 MeV, and has been fully used in this work. The only exception is for neutron inelastic scattering from ^{12}C at 94.8 MeV. Therefore, we limited our incident energy range to 100 keV $< E <$ 30 MeV.

Using the SFRESCO code, we simultaneously predicted the elastic and inelastic angular distributions by using our model parameters given in Eqs. (22) for incident neutron energies in the range 10 MeV $\leq E \leq$ 30 MeV. For permanently deformed nuclei, the non-diagonal part of the optical potential couples the ground state to the inelastic excited states

[20]. Consequently, we included the deformation parameters in the fitting the experimental data of the coupled channels differential cross sections for collective excitation. Our obtained best-fit values are shown in Table 1 together with the coupled excitation levels. Below 10 MeV, we used the TALYS code with our potential parameters given in Eq. (22) to predict the experimental data as TALYS uses the Hauser - Feshbach theory [28] to account for compound nucleus formation. To simplify the presentation we divide this section into two parts; the first deals with the results of the intermediate and heavy nuclei and the second part deals with extending our model to the case of light nuclei.

4.1. Medium and heavy nuclei

Unlike light nuclei, in this section we consider coupling the elastic channel to one and two excited states simultaneously for medium and heavy nuclei have skin thickness regions that form small part of the nuclear volume. Therefore, surface effects which usually result in potential parameters that show large energy dependence are expected to play a reduced role. For $24 \leq A \leq 238$, a volume imaginary part $W_v(E)$, as given in Eq. (22), resulted in a marked improvement in the overall agreement between the predictions of our model and the experimental data. In particular, it improved the predictions of the first elastic angular distribution minima especially for ^{54,56}Fe target nucleus. The volume term was also found important in improving the elastic angular distribution fits corresponding to neutron scattering from ^{208}Pb [38].

Coupling the elastic to inelastic channels for the medium from ^{24}Mg to ^{65}Cu nuclei

Here, For ^{24}Mg, the 0^+ ground state is coupled to the 2^+ (1.368 MeV) inelastic channel, For ^{28}Si the 0^+ ground state is coupled to the $2^+(1.779)$, $4^+(4.617$ MeV), and 3^- (6.878 MeV) inelastic channels, For ^{32}S the 0^+ ground state is coupled to the $2^+(2.230$ MeV), and 3^- (5.010 MeV) inelastic channels, For ^{40}Ca the 0^+ ground state is coupled to the $3^-(3.736$ MeV) inelastic channel. For ^{51}V the $7/2^-$ ground state is coupled to the $3/2^-(0.982$ MeV) inelastic channel. For ^{52}Cr the 0^+ ground state is coupled to the $2^+(1.434$ MeV) inelastic channel.

Our predictions for the elastic and inelastic differential cross sections are in very good agreement with the measured data as can be seen in Figs. 2 to 3. We have considered even - even and odd A target nuclei. Depending on the availability of the inelastic scattering data we have coupled the ground state to one, two and three inelastic excited channels. For low incident neutron energies, we found the vibrational model to result in a slightly better agreement with experiment than the rotational model. Also, For ^{54}Fe, the 0^+ ground state is coupled to the 2^+ (1.408 MeV) inelastic channel, For ^{56}Fe the 0^+ ground state is coupled to the $2^+(0.846)$, $4^+(3.122$ MeV), and $3^-(4.51$ MeV) inelastic channels, For ^{58}Ni, the 0^+ ground state is coupled to the $2^+(1.454$ MeV) inelastic channel, For ^{60}Ni, the 0^+ ground state is coupled to the $2^+(1.333$ MeV), and 3^- (4.039 MeV) inelastic channels For ^{63}Cu the $3/2^-$ ground state is coupled to the $7/2^-(1.327$ MeV) inelastic channel, For ^{65}Cu the $3/2^-$ ground state is coupled to the $7/2^-(1.481$ MeV) inelastic channel, Inspection of Figs. 4-9 shows that the predicted angular distributions are in very good agreement with experiment. We particularly note that the predictions of the first-order diffraction minima for ^{54}Fe and ^{56}Fe were significantly improved by introducing a volume imaginary term as given in Eq. (22). In addition, since experimental polarization data is available, we used the optimized optical potential parameters to calculate the analyzing power. As can be seen in Figs. 7 and 8 for ^{54}Fe and ^{58}Ni the theoretical predictions are in very good agreement with the data.

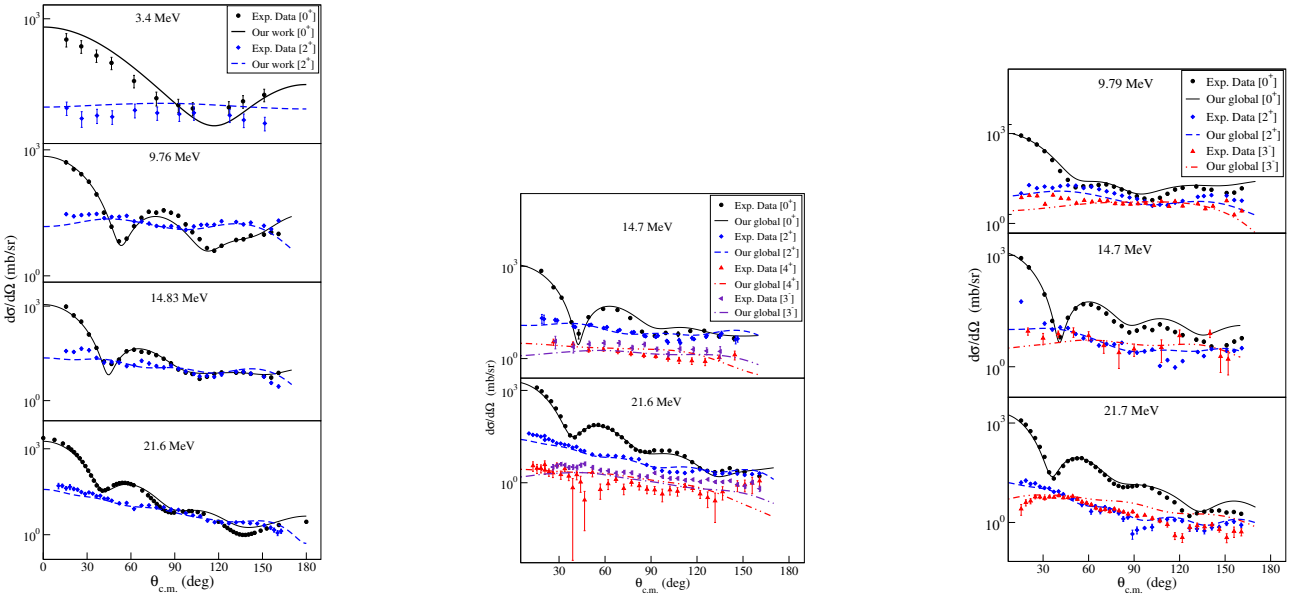

Figure 2. (Color online)Comparison between experimental angular distributions and results of OMP calculations with coupled channles computations for neutron elastic and inelastic scattering from ^{24}Mg (left), ^{28}Si (middle), and ^{32}S (right).

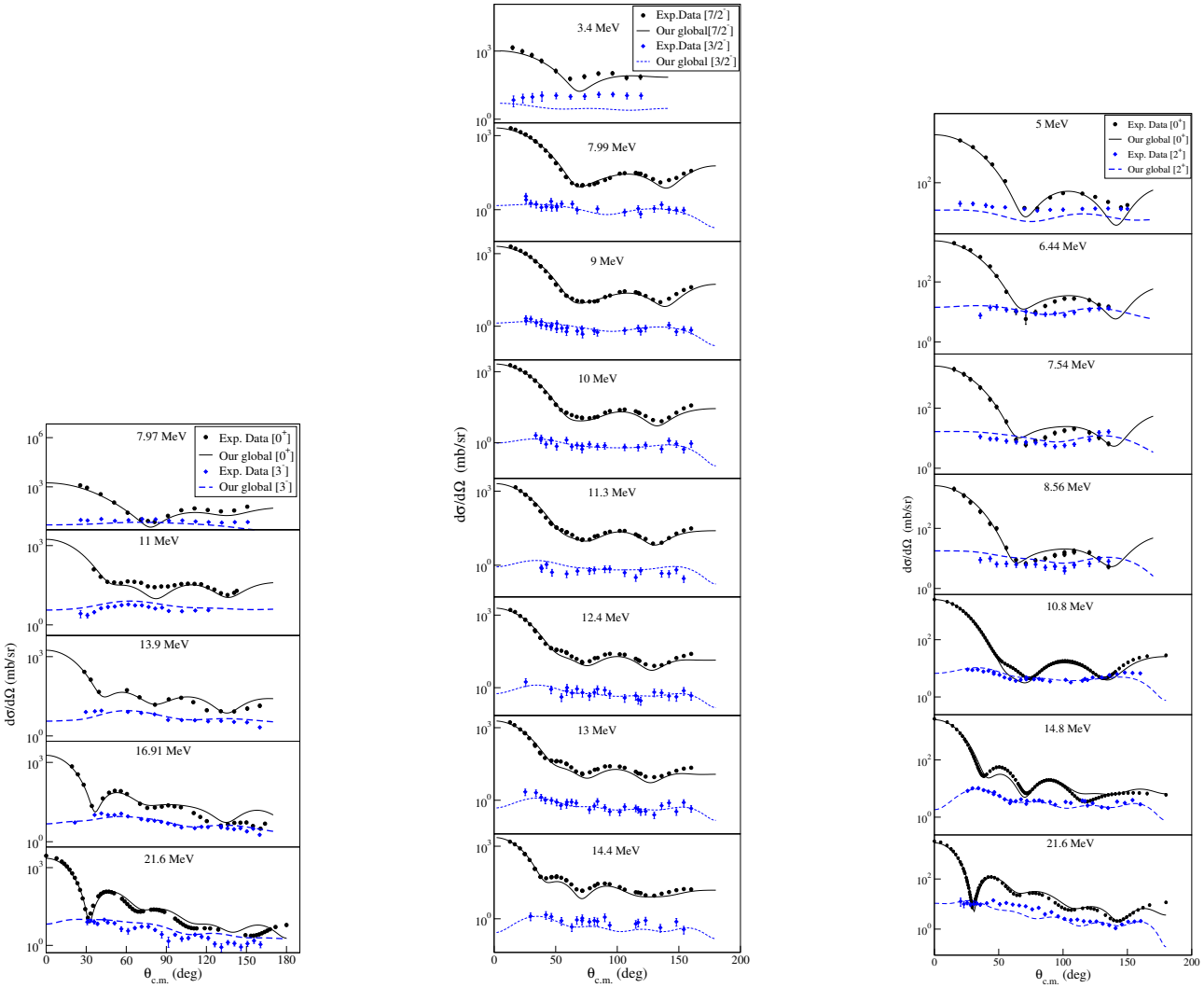

Figure 3. (Color online) Comparison between experimental angular distributions and results of OMP calculations with coupled channles computations for neutron elastic and inelastic scattering from ^{40}Ca (left), ^{51}V (middle), and ^{52}Cr (right).
.

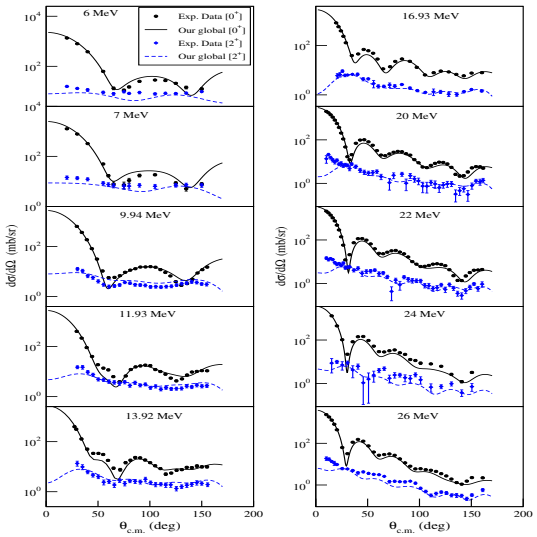

Figure 4. (Color online) Comparison between experimental angular distributions and results of OMP calculations with coupled channles computations for neutron elastic and inelastic scattering from ^{54}Fe.

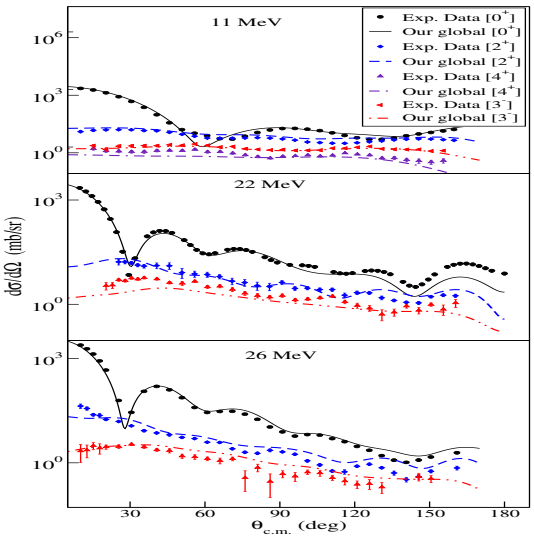

Figure 5. (Color online) Comparison between experimental angular distributions and results of OMP calculations with coupled channles computations for neutron elastic and inelastic scattering from ^{56}Fe.

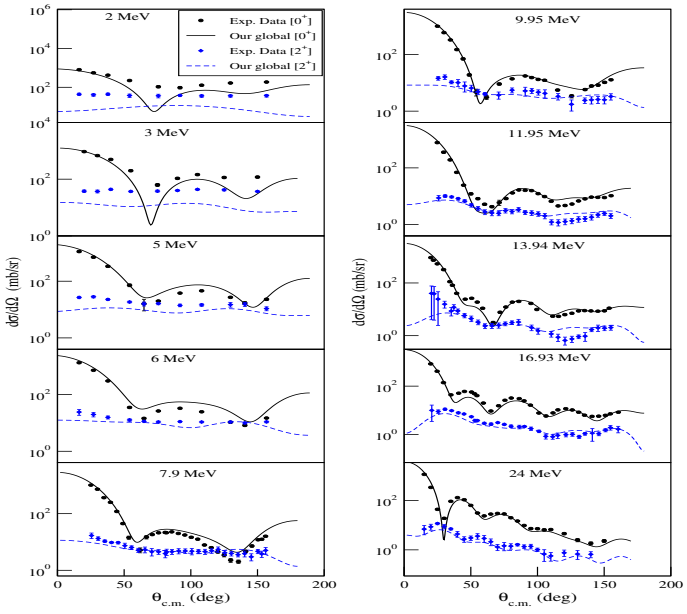

Figure 6. (Color online) Comparison between experimental angular distributions and results of OMP calculations with coupled channles computations for neutron elastic and inelastic scattering from ^{58}Ni.

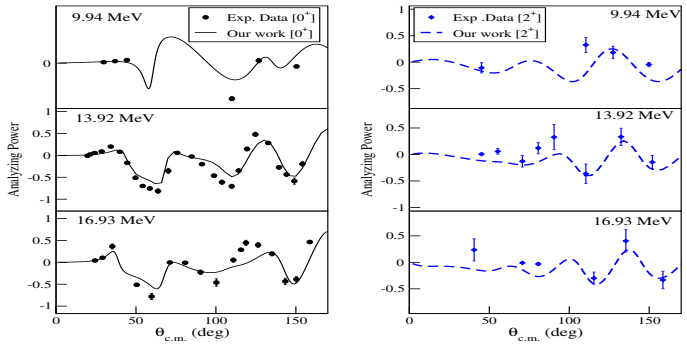

Figure 7. (Color online) Comparison of the theoretical predictions for the analyzing power with experimental data for ^{54}Fe$(n,n)^{54}$Fe*.

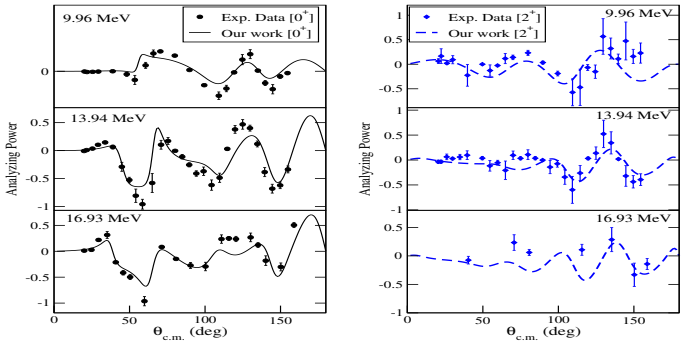

Figure 8. (Color online) Comparison of the theoretical predictions for the analyzing power with experimental data for ^{58}Ni$(n,n)^{58}$Ni*.

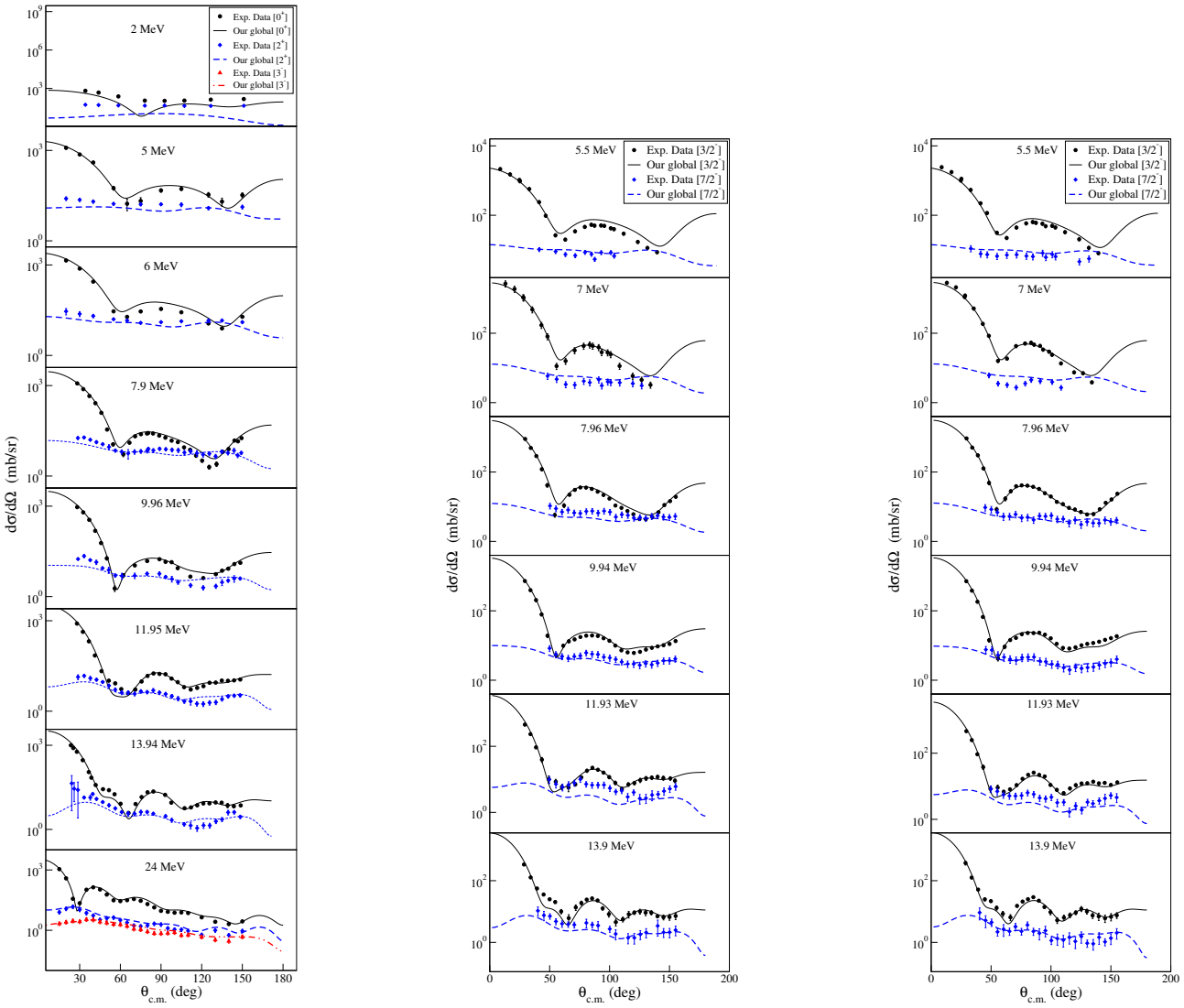

Figure 9. (Color online) Comparison between experimental angular distributions and results of OMP calculations with coupled channles computations for neutron elastic and inelastic scattering from ^{60}Ni (left), ^{63}Cu (middle), and ^{65}Cu (right).

Coupling the elastic to inelastic channels for the heavy from ^{76}Se to ^{238}U nuclei

In this section, for ^{76}Se, the 0^+ ground state is coupled to the 2^+ (0.559 MeV) inelastic channel, For ^{80}Se the 0^+ ground state is coupled to the 2^+(0.666) MeV inelastic channel, For ^{90}Zr the 0^+ ground state is coupled to the 2^+(2.19 MeV) inelastic channel, For ^{92}Zr the 0^+ ground state is coupled to the 2^+(0.935 MeV) inelastic channel, For ^{94}Mo the 0^+ ground

state is coupled to the 2^+(0.871 MeV) inelastic channel. As for the previous nuclei, our theoretically calculated angular distributions for neutron scattering off ^{76}Se, ^{80}Se, ^{90}Zr, ^{92}Zr, and ^{94}Mo nuclei are in good agreement with experimental data as can be seen in Figs. 10 - 11. Also, For ^{116,118,120}Sn, the 0^+ ground state is coupled to the 2^+ (1.293, 1.229, 1.171 MeV), and 3^- (2.266, 2.324, 2.400 MeV) inelastic channels respectively, For ^{208}Pb the 0^+ ground state is coupled to the 3^-(2.615) MeV, 5^-(3.197 MeV) inelastic channels, For ^{238}U the 0^+ ground state is coupled to the 2^+(0.045 MeV), and 4^+ (0.148 MeV) inelastic channels, Inspection of Figs. 12-13 shows that our predicted angular distributions for neutron scattering off ^{116,118,120}Sn, ^{208}Pb and ^{238}U nuclei are in good agreement with experiment.

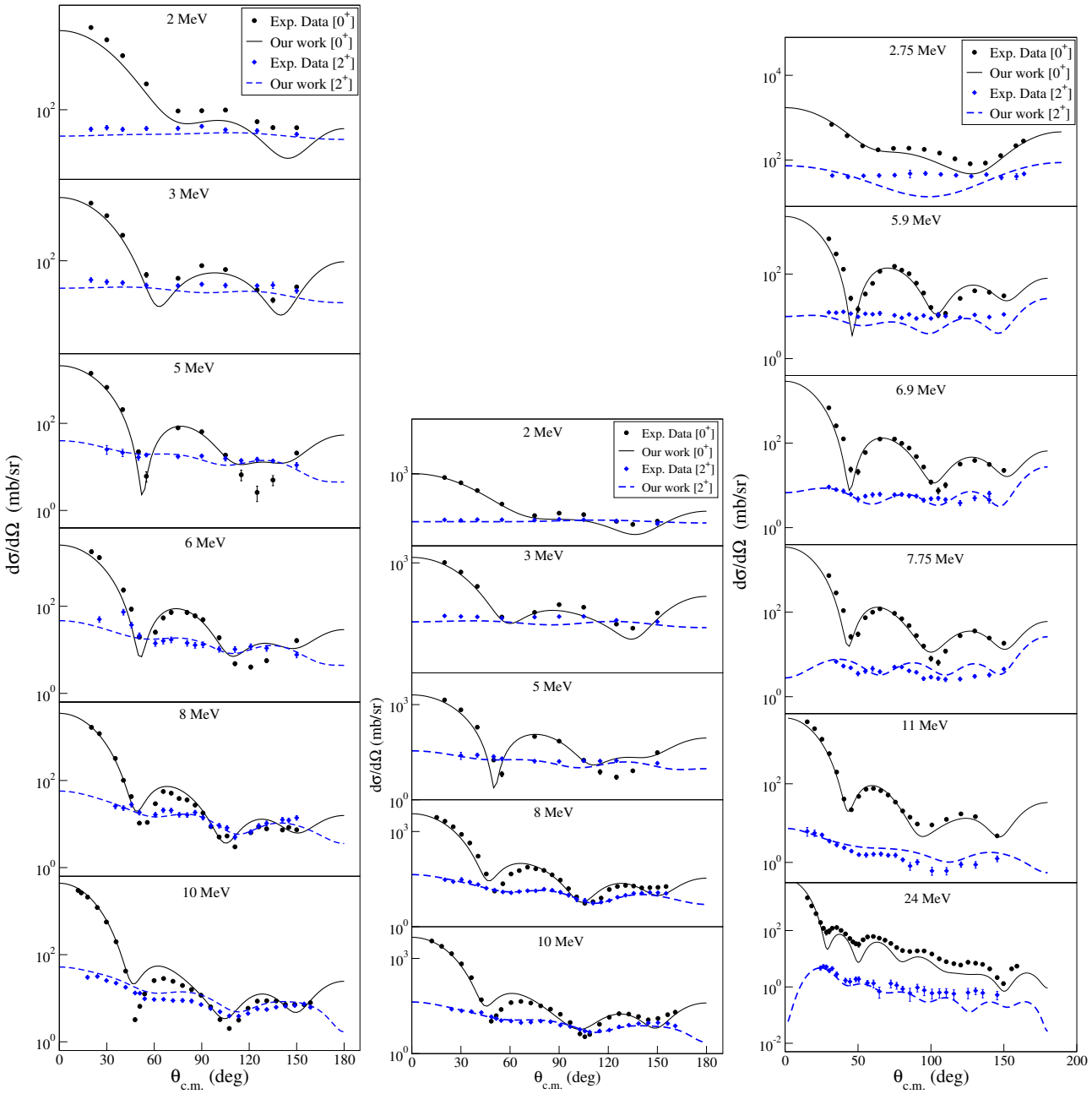

Figure 10. (Color online) Comparison between experimental angular distributions and results of OMP calculations with coupled channles computations for neutron elastic and inelastic scattering from ^{76}Se (left), ^{80}Se (middle) , and ^{90}Zr (right).

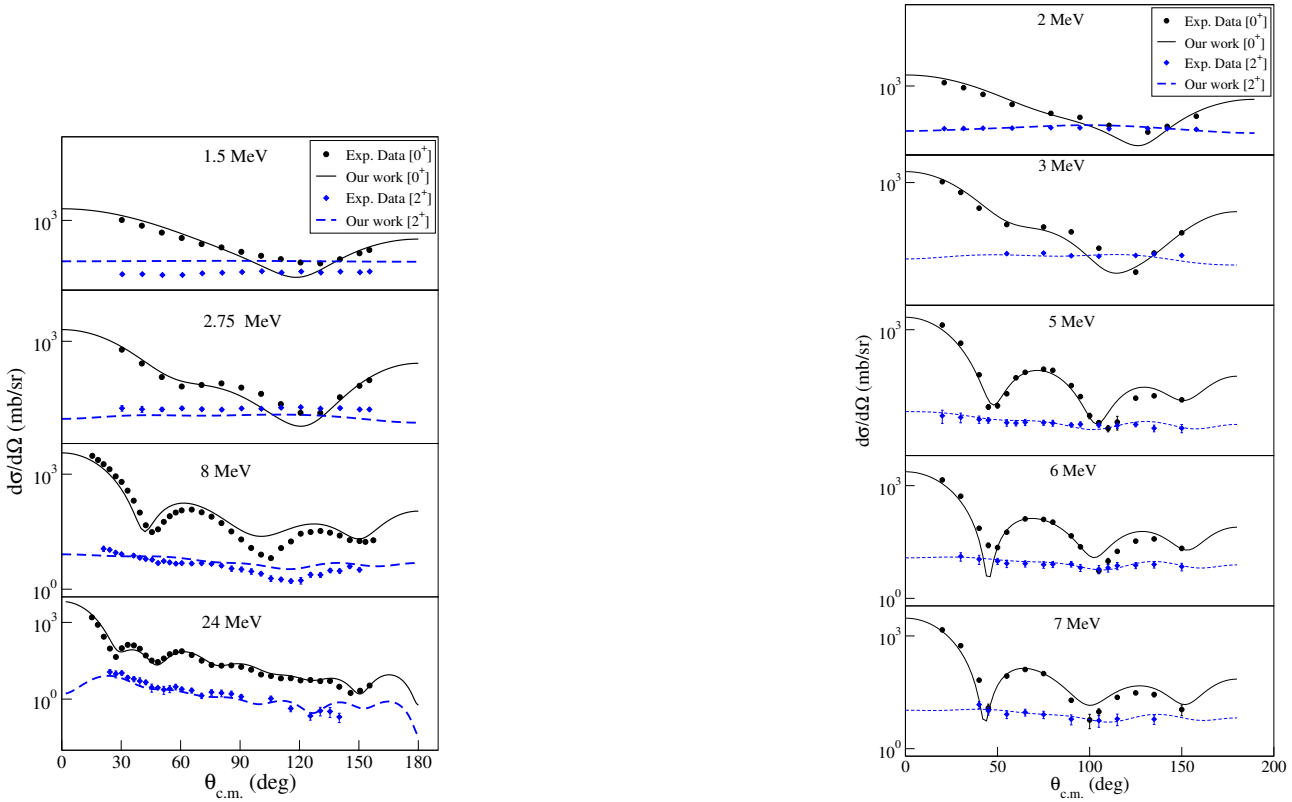

Figure 11. (Color online) Comparison between experimental angular distributions and results of OMP calculations with coupled channles computations for neutron elastic and inelastic scattering from ^{92}Zr (left) and ^{94}Mo (right).

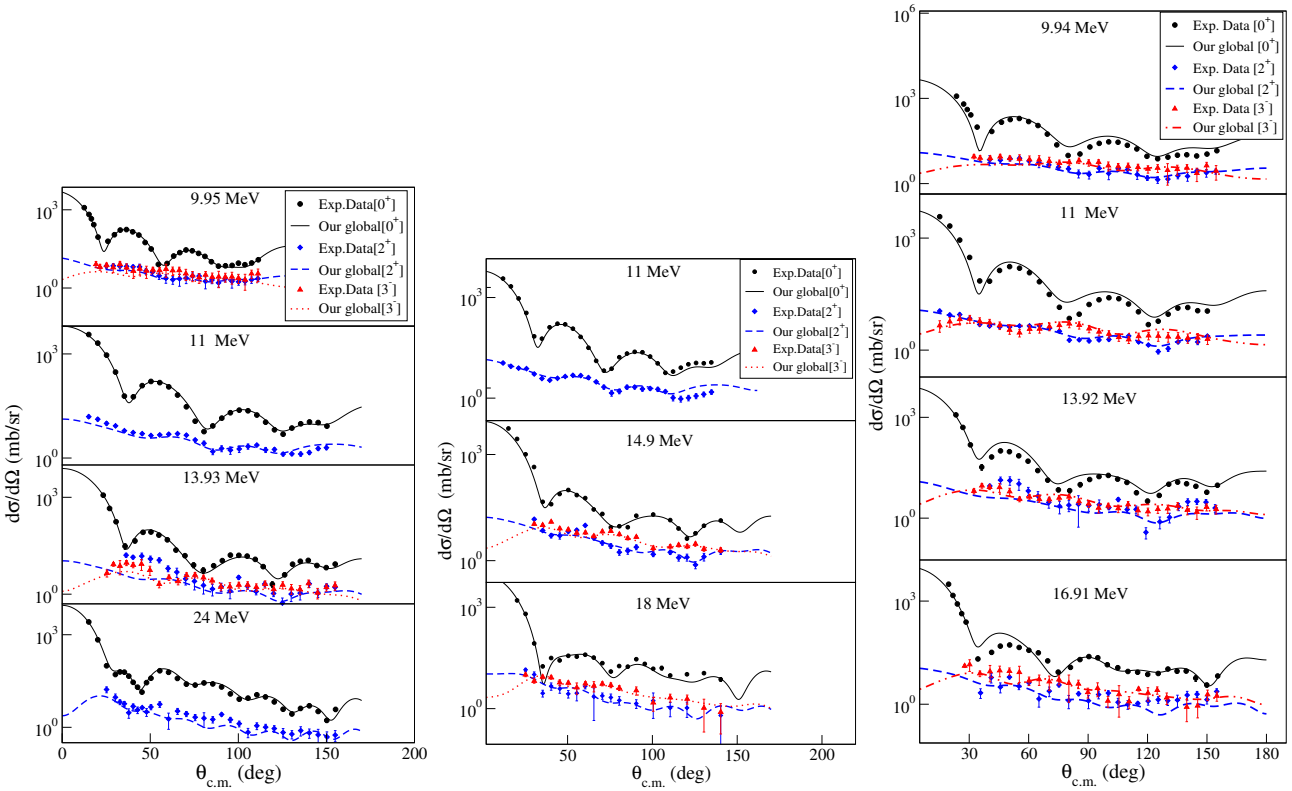

Figure 12. (Color online) Comparison between experimental angular distributions and results of OMP calculations with coupled channles computations for neutron elastic and inelastic scattering from ^{116}Sn (left) , ^{118}Sn (middle), and ^{120}Sn (right).

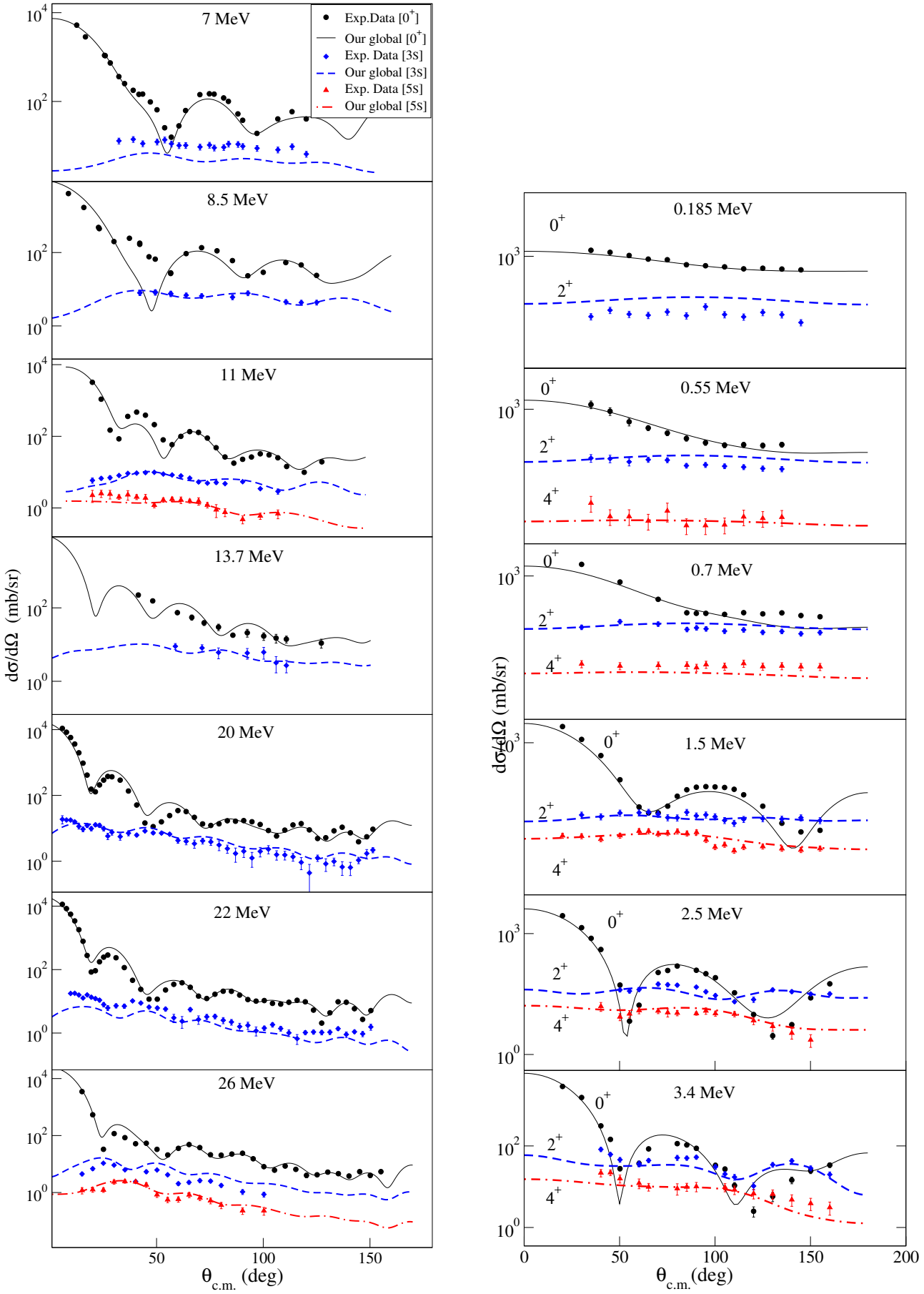

Figure 13. (Color online) Comparison between experimental angular distributions and results of OMP calculations with coupled channles computations for neutron elastic and inelastic scattering from ^{208}Pb (left) and ^{238}U (right).

4.2. Extending the model to the case of light nuclei

In this section we test the applicability of our model to the light ^{6}Li, ^{12}C and ^{16}O target nuclei, which differ from the intermediate and heavy ones in that the surface region makes up a large portion of the nuclear volume. For the $n - ^{6}$ Li scattering process, inelastic angular distribution data are available only for coupling the 1^{+} ground state to the 3^{+} (2.186 MeV) excited state. also we shall consider coupling the 0^{+} ground state of ^{12}C to the 2^{+} (4.438 MeV) and 3^{-} (9.641 MeV) excited states simultaneously. Similarly, the 0^{+} ground state of the ^{16}O nucleus is simultaneously coupled to the 3^{-} (6.129 MeV) and 2^{+} (6.917 MeV) excited states. This results in structural effects in the angular distributions that are manifested as prominent minima in the elastic angular distributions, particularly, at large scattering angles. This has always resulted in difficulties in predicting the experimental data even when developing local optical potentials [11] - [16]. As can be seen in Eq. (22), the smooth functional forms corresponding to ^{6}Li are the same as those for the intermediate nuclei. However, for ^{12}C and ^{16}O best predictions could only be obtained by shifting the imaginary surface absorption term by a constant compared to the rest of the nuclei considered in this work as displayed in Eq. (22). Despite the difficulties encountered when dealing with light nuclei, and taking into account that the spin - orbit depths and all the geometrical parameters are fixed, figures 14 - 15 show that our predictions for the angular distributions, particularly the elastic ones, are in very good overall agreement with the experimental data.

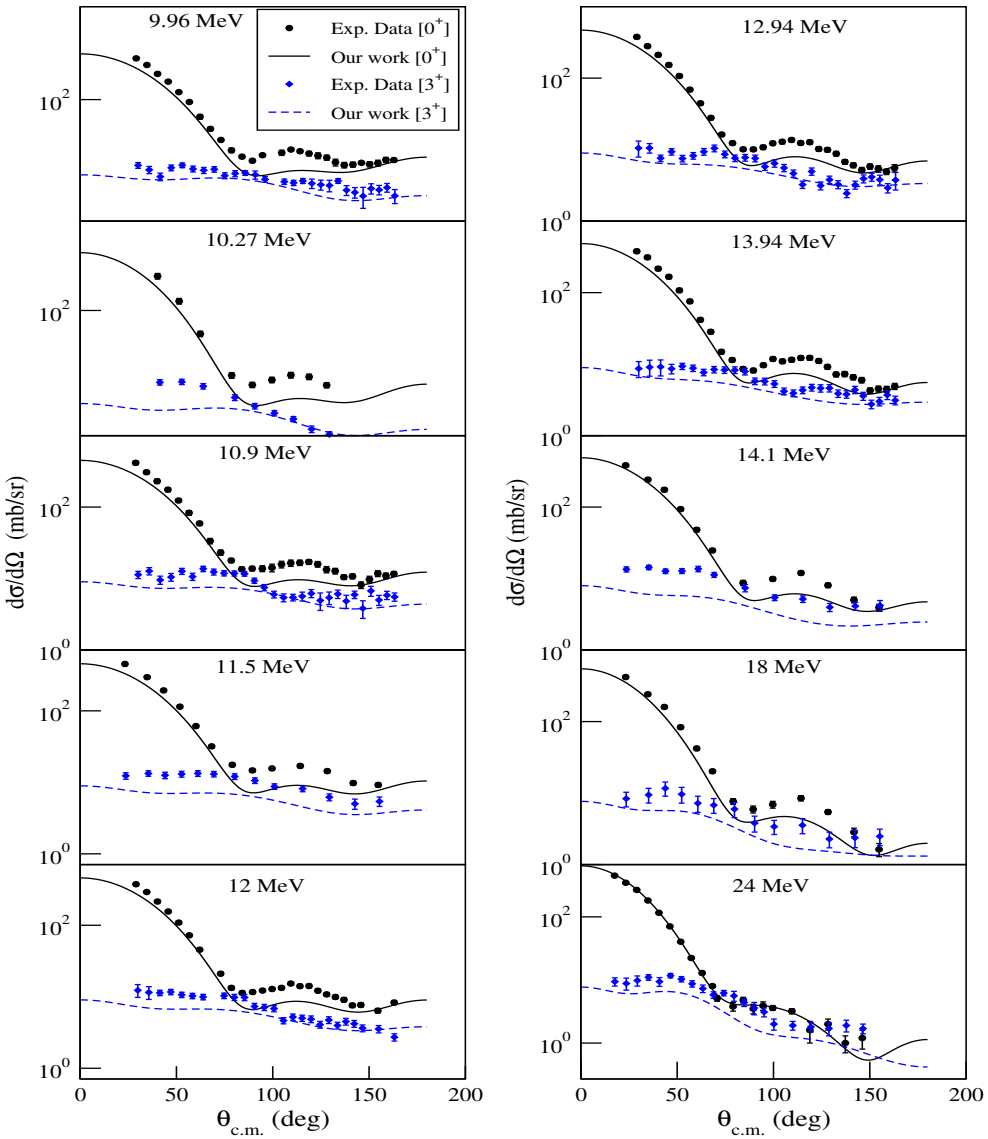

Figure 14. (Color online) Comparison between experimental angular distributions and results of OMP calculations with coupled channles computations for neutron elastic and inelastic scattering from ^{6}Li.

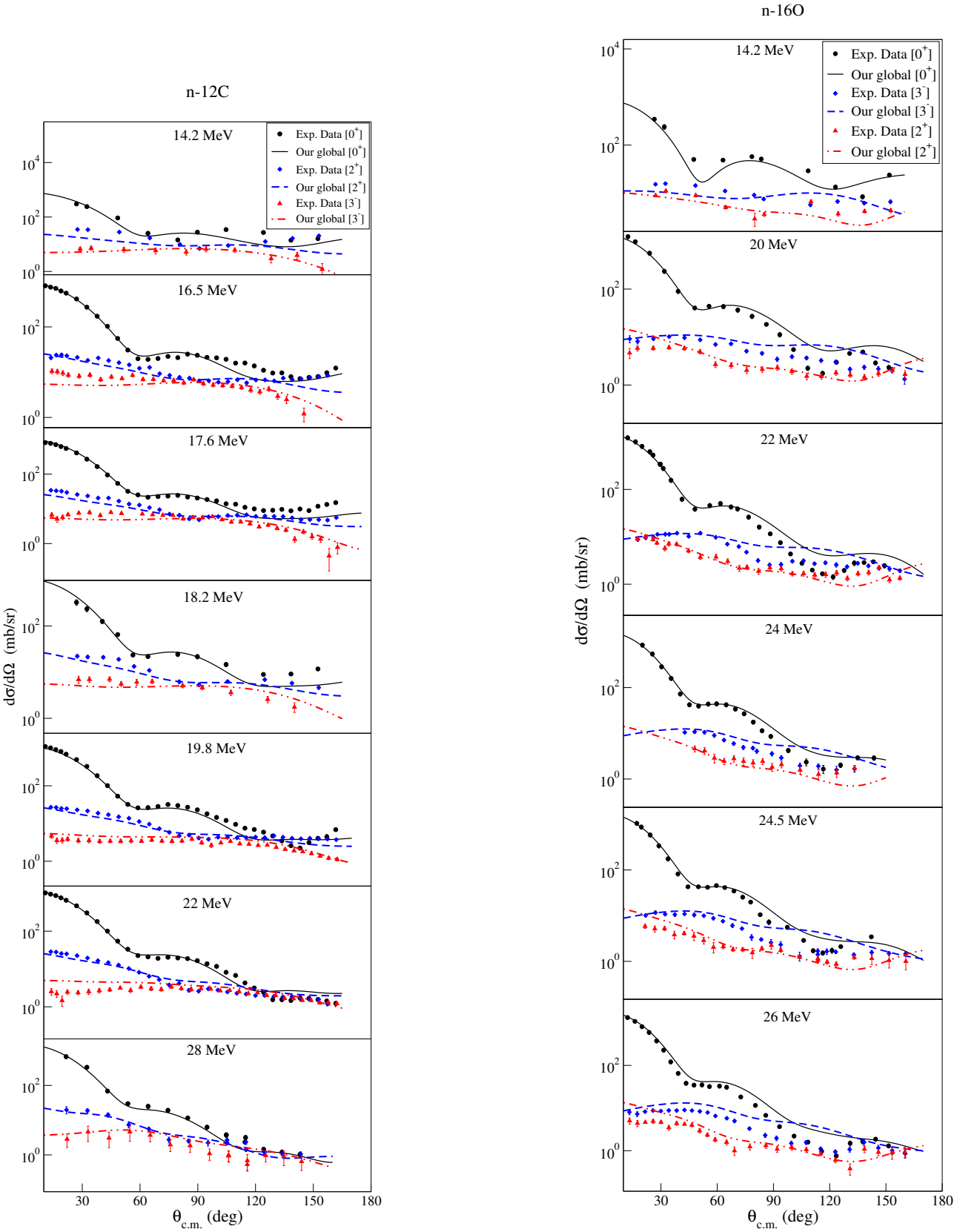

Figure 15. (Color online) Comparison between experimental angular distributions and results of OMP calculations with coupled channles computations for neutron elastic and inelastic scattering from ^{12}C (left) and ^{16}O (right).

5. TOTAL CROSS SECTIONS

In Figs. 16 and 17 we compare our predictions for the total and total elastic cross sections with the experimental values. For the medium and heavy nuclei, our theoretical predictions for the cross sections are in good overall agreement with the data. In general, the agreement becomes progressively better with increasing mass number of the target nucleus. It is also worth noting that the introduction of a volume imaginary term $W_v(E)$ for the nuclei $6 \leq A \leq 238$, as given in Eq. (22), significantly improved our predictions. The attempt to include light nuclei in our analysis has been more successful in predicting the angular distributions than predicting the total cross sections. For the light ^{6}Li nucleus, the agreement between the theoretical and experimental values is better at energies above 10 MeV as can be seen in Fig. 16. A similar behavior was also observed for the ^{12}C and ^{16}O nuclei. As we mentioned above, this could be a consequence of structural effects that play an important role in the nucleon scattering process from such light nuclei [21] and [37]. In fact, in an earlier work, we developed local optical potential fits where all the potential parameters were allowed to vary with energy and target mass number. The calculated total and total elastic cross sections for carbon and oxygen still showed some discrepancy with experimental data [21]. Clearly, our attempted case of developing smooth functional forms for the potential depths, keeping the geometrical parameters and spin -orbit term fixed is even more difficult. This difficulty is confirmed by noting that the differential cross section for nucleon elastic scattering from ^{16}O shows a minimum around 120^{0} which could not be fitted despite many attempts using local and microscopic optical potentials [39]. Finally, the measured data were taken from the Evaluated Nuclear Data File [ENDF] except the values of the total cross sections for ^{6}Li and ^{12}C which were obtained from [EXFOR].

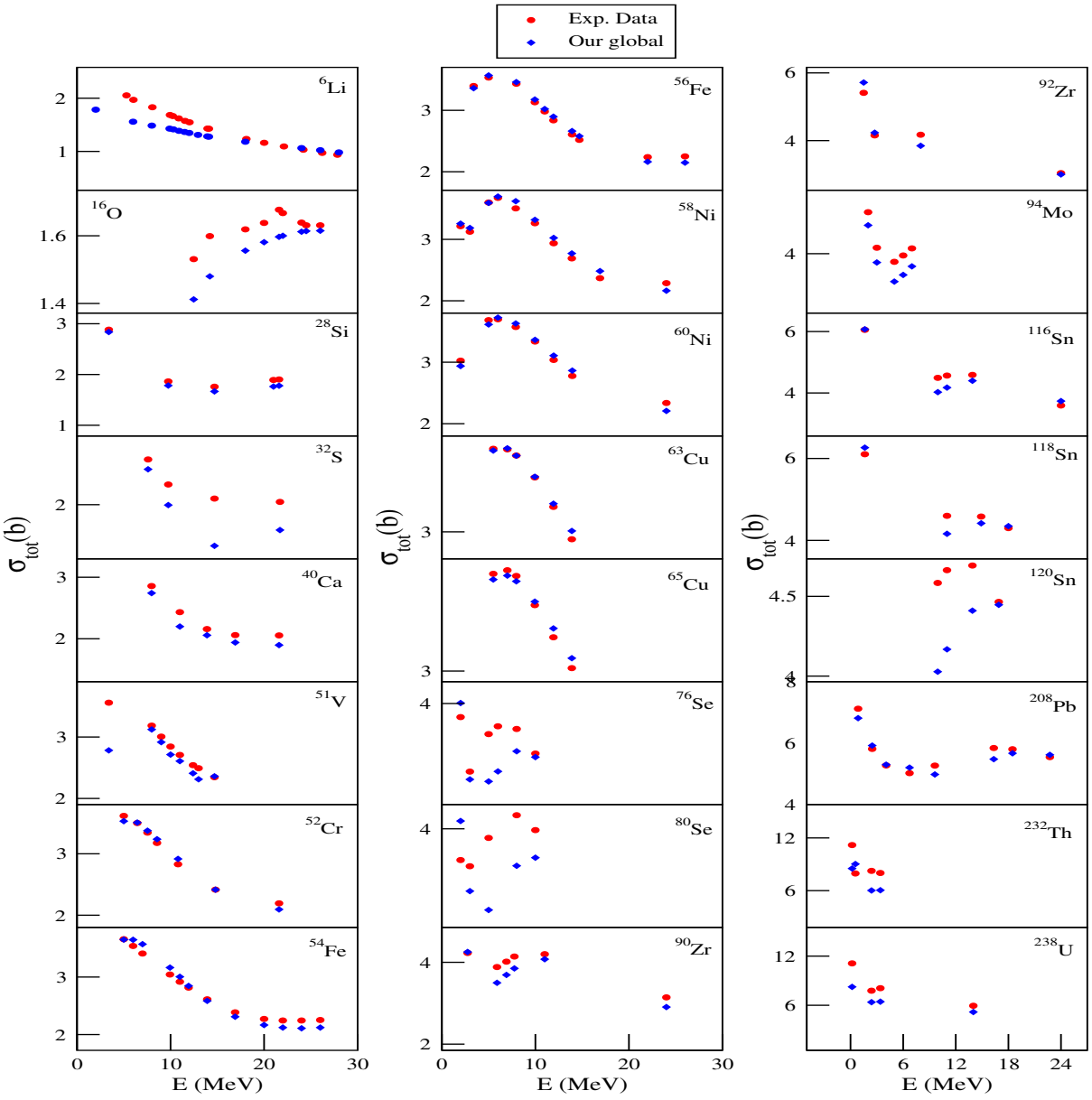

Figure 16. (Color online) Comparison of predicted neutron total cross sections and experimental data from ^{6}Li to ^{238}U.

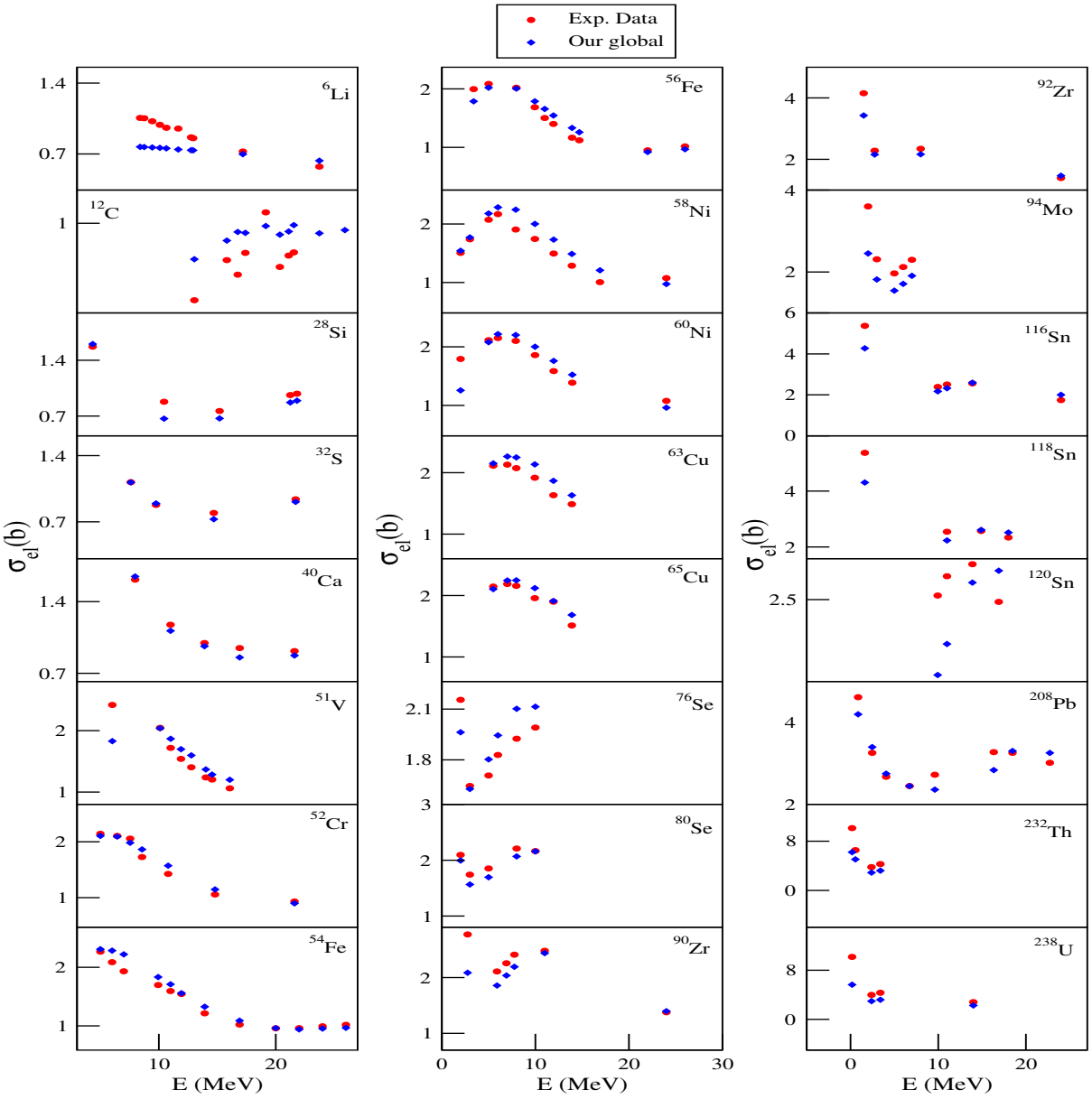

Figure 17. (Color online) Comparison of predicted neutron elastic cross sections and experimental data from ^{6}Li to ^{238}U.

6. CONCLUSIONS

In this work we investigated neutron scattering from medium and heavy nuclei using an optical model with channel coupling. We also tested the applicability of our model to the case of light nuclei. Therefore, we considered nuclear targets from ^{6}Li to ^{238}U and incident neutron energies in the range 180 keV $< E <$ 30 MeV. No higher energies were investigated as there are no experimental inelastic angular distribution data for the nuclei studied in this work. We obtained smooth functional forms for the real volume, imaginary volume and the imaginary surface depths as functions of energy, mass number and the neutron - proton asymmetry of the target nucleus as given in Eq. (22).

Using our optimized set of parameters, we simultaneously predicted the elastic and inelastic angular distribution data. As can be seen in Figs. 2 to 9 and 10 to 13, for the intermediate and heavy nuclei, our calculated values are in very good overall agreement with the experimental data. The predicted polarization data are also in very good agreement with the experimental values as can be seen in Figs. 7 and 8. Our model has also been extended to predict the elastic and inelastic angular distributions for the light ^{6}Li, ^{12}C and ^{16}O nuclei which, unlike intermediate and heavy nuclei, have diffuse edges and less uniform matter distributions that complicate the process of predicting the experimental data. Despite this, The calculated angular distributions show a very reasonable overall agreement with the experimental data as can be seen by inspecting Figs. 14 to 15.

In addition, we calculated total and total elastic cross sections. Our theoretical predictions are in good agreement with the corresponding experimental values particularly for the intermediate and heavy nuclei. This agreement becomes

increasingly better with increasing mass number of the target nucleus. In fact, the introduction of (i) an imaginary volume term W_v for the nuclei with mass numbers $6 \leq A \leq 238$ and (ii) shifting the imaginary surface term by a constant for light nuclei, as can be seen in Eq. (22), significantly improved the predicted angular distributions and total cross sections. As for the light ^{6}Li, ^{12}C and ^{16}O nuclei, our calculations show better agreement for incident energies above 10 MeV. The discrepancy below 10 MeV incident energy could be a result of structural effects playing an important role in the scattering process [21] and [37]. For light nuclei, our model has been more successful in predicting the elastic and inelastic angular distributions than total cross sections.

ORCID

Waleed Saleh Alrayashi, https://orcid.org/0009-0009-6440-8332

REFERENCES

[1] H. Feshbach, Ann. of Phys. **5**, 357 (1958). https://doi.org/10.1016/0003-4916(58)90007-1

[2] A.J. Koning, and J.P. Delaroche, Nucl. Phys. A, **713**, 231 (2003). https://doi.org/10.1016/S0375-9474(02)01321-0

[3] Y. Han, Y. Xu, H. Liang, H. Guo, and Q. Shen, Phys.Rev. C, **81**, 024616 (2010).https://doi.org/10.1103/PhysRevC.81.024616

[4] S. Kunieda, S. Chiba, K. shibata, A. Ichihara, and E.Sh. Sukhovitski, Journal of nuclear science and technology, **44**(6), 838 (2007). https://doi.org/10.1080/18811248.2007.9711321

[5] I.J.Thompson, and F.M. Nunes, *Nuclear reactions for Astrophysics*, (Cambridge University Press, 2009).

[6] G. Racah, Phys. Rev. **62**, 438 (1942). https://doi.org/10.1103/PhysRev.62.438

[7] J.M. Eisenberg, and W. Greiner, *Nuclear Models*, Vol. 1, Ch. 2, (North-Holland, 1970).

[8] A. Saleh, and M.I. Jaghoub, Phys. Rev. C, **109**, 034606 (2024). https://doi.org/10.1103/PhysRevC.109.034606

[9] A. Albelleh, M.I. Jaghoub, and W.S. Al-Rayashi, Nucl. Phys. A, **1024** , 122461 (2022). https://doi.org/10.1016/j.nuclphysa.2022.122461

[10] S. Alameer, M.I. Jaghoub, and I, Ghabar, J. Phys. G: Nucl. Part. Phys. **49**, 015106 (2022). https://doi.org/10.1088/1361-6471/ac38c2

[11] I.N. Ghabar, and M.I. Jaghoub, Phys. Rev. C, **91**, 064308 (2015). https://doi.org/10.1103/PhysRevC.91.064308

[12] M. Utoom, M.I. Jaghoub, and T. Aqel, Can. J. Phys. **100** , 015106 (2022). https://doi.org/10.1139/cjp-2021-0380

[13] T. Aqel, M.I. Jaghoub, Eur. Phys. J. A, **56**, 216 (2020). https://doi.org/10.1140/epja/s10050-020-00226-5

[14] T. Aqel, M.I. Jaghoub, Nucl. Phys. A, **989**, 145 (2019). https://doi.org/10.1016/j.nuclphysa.2019.06.005

[15] M.I. Jaghoub, A.E. Lovell, and F.M. Nunes, Phys. Rev. C, **98**, 024609 (2018). http://dx.doi.org/10.1103/PhysRevC.98.024609

[16] J. Klug, J. Blomgren, A. Atac, B. Bergenwall, A. Hildebrand, C. Johansson, P. Mermod, *et al.*, Phys. Rev. C, **68**, 064605 (2003). https://doi.org/10.1103/PhysRevC.68.064605

[17] H. An, and C. Cai, Phys. Rev. C, **73**, 054605 (2006). https://doi.org/10.1103/PhysRevC.73.054605

[18] A. Bohr, and B.R. Mottelson, Kgl. Danske Videnskab. Selskab, Mat. Fys. Medd. **27**(16), (1953). https://cds.cern.ch/record/213298/files/p1.pdf

[19] D.M. Chase, L. Wilets, and A.R. Edmonds, Rotational-Optical Model For Scattering of Neutrons Phys. Rev. **110**, 1080 (1985). https://doi.org/10.1103/PhysRev.110.1080

[20] T. Tamura, Rev. Mod. Phys. **37**, 679 (1965). https://doi.org/10.1103/RevModPhys.37.679

[21] W.S. Al-Rayashi, and M.I. Jaghoub, Phys. Rev. C, **93**, 064311 (2016). https://doi.org/10.1103/PhysRevC.93.064311

[22] B. Buck, Phys. Rev. **130**, 712 (1963). https://doi.org/10.1103/PhysRev.130.712

[23] M.P. Fricke, E.E. Gross, B.J. Mortgn, and A. Zucker, Phys. Rev. **156**, 1207 (1967). https://doi.org/10.1103/PhysRev.156.1207

[24] S. Chiba, K. Shibata, A. Ichihara, and F.Sh. Sukhovitsi $\tilde{i}$, Journal of nuclear sciences and technology, **44**(6), 838 (2007). https://doi.org/10.1080/18811248.2007.9711321

[25] G. Haouat, Ch. Lagrange, R. de Swiniarski, F. Dietrich, J.P. Delaroche, and Y. Patin, Phys. Rev C, **30**, 1795 (1984). https://doi.org/10.1103/PhysRevC.30.1795

[26] I.J. Thompson, Coupled Reaction Channels Calculations in Nuclear Physics, Computer Physics Reports, **7**, 167 (1988). https://doi.org/10.1016/0167-7977(88)90005-6

[27] A.J. Koning, S. Hilaire, and M.C. Duijvestijn, "TALYS-1.0", in: *Proceedings of the International Conference on Nuclear Data for Science and Technology*, edited by O. Bersillon, F. Gunsing, E. Bauge, R. Jacqmin, and S.Leray, (EDP Sciences, Nice, France, 2008), pp. 211-214. https://doi.org/10.1051/ndata:07767

[28] W. Hauser, and H. Feshbach, Phys. Rev. **87**, 366 (1952). https://doi.org/10.1103/PhysRev.87.366

[29] S. Cwiok, J. Dudek, W. Nazarewicz, J. Skalski, and V. Werner, Comput. Phys. Commun. **46**, 379 (1987). https://doi.org/10.1016/0010-4655(87)90093-2

[30] G.M. Crawley, and G.T. Garvey, Phys. Rev. **160**, 981 (1967). https://doi.org/10.1103/PhysRev.160.981

[31] S. Raman, C.W. Nestor, Jr.S. Kahane, and K.H. Bhatt, Phys. Rev. C, **43**, 556 (1991). https://doi.org/10.1103/PhysRevC.43.556

[32] L. Grodzins, Phys. Lett. **2**, 88 (1962). https://doi.org/10.1016/0031-9163(62)90162-2

[33] M.P. Fricke, and G.R. Satchler, Phys. Rev. **139**, B567 (1965). https://doi.org/10.1103/PhysRev.139.B567

[34] R.A. Zureikat, and M.I. Jaghoub, Nucl. Phys. A, **916**, 183 (2013). https://doi.org/10.1016/j.nuclphysa.2013.08.007

[35] EXFOR: Experimental Nuclear Reaction Data, https://www-nds.iaea.org/exfor/exfor.htm

[36] CINDA: Computer Index of Nuclear Reaction Data https://www-nds.iaea.org/exfor/cinda.htm

[37] A. Bonaccorso, and R.J. Charity, Phys. Rev. C, **89**, 024619 (2014). https://doi.org/10.1103/PhysRevC.89.024619

[38] R.W. Finlay, J.R.M. Armand, T.S. Cheema, J. Rapaport, and F.S. Dietrich, Phys. Rev. C, **30**, 796 (1984). https://doi.org/10.1103/PhysRevC.30.796

[39] G.H. Rawitscher, and D. Lukaszek, Phys. Rev. C, **69**, 044608 (2004). https://doi.org/10.1103/PhysRevC.69.044608

ПОТЕНЦІАЛ ФЕНОМЕНОЛОГІЧНОЇ ОПТИЧНОЇ МОДЕЛІ ГЛОБАЛЬНОГО ЗВ'ЯЗАНОГО КАНАЛУ ДЛЯ НЕЙТРОННО-ЯДЕРНОГО РОЗСІЮВАННЯ ВІД ^{6}Li ДО ^{238}U

Валід Салех Алраяші

Департамент науки, факультет освіти, Університет Сани, Сана, Ємен

Вважається, що процес нейтронно-ядерного розсіювання створює гладкі функціональні форми для реальної та уявної частин феноменологічного оптичного потенціалу з використанням формалізму аналізу зв'язаних каналів. Ми розглядаємо проміжні та важкі ядерні мішені та досліджуємо можливість розширення моделі на зазвичай виключений випадок легких ядер. Використовуючи нашу модель, ми одночасно прогнозуємо пружні та непружні кутові розподіли розсіювання нейтронів від ^{6}Li до ^{238}U для різних енергій у діапазоні 100 кеВ $< E <$ 30 МеВ, для яких доступні дані про непружні кутові розподіли. Ми отримуємо гладкі форми для реальних і уявних глибин об'ємних і поверхневих потенціалів як функцій енергії, масового числа та асиметрії між числами протонів і нейтронів у ядрі-мішені. Глибини реального та уявного спін-орбітального члена та всі геометричні параметри потенціалу фіксовані. Наші прогнозовані пружні та непружні диференціальні поперечні перерізи дуже добре узгоджуються з виміряними даними. Розраховані загальні пружні, загальні поперечні перерізи та аналізуючі здібності в цілому добре узгоджуються з експериментальними значеннями, особливо для проміжних і важких ядер.

Ключові слова: *потенціал оптичної моделі; пружне розсіювання; непружне розсіювання; зв'язані канали; диференціальний переріз*